SLAC-PUB-9976

SEARCH FOR MILLI-CHARGED PARTICLES AT SLAC

W.G.J. Langeveld*
Stanford Linear Accelerator Center, Stanford University, Stanford, California 94309

Representing the mQ Collaboration

ABSTRACT

Particles with electric charge $q \equiv Qe \leq 10^{-3}\, e$ and masses in the range 1–1000 MeV/c^2 are not excluded by present experiments or by astrophysical or cosmological arguments. A beam dump experiment uniquely suited to the detection of such "millicharged" particles has been carried out at SLAC, utilizing the short-duration pulses of the SLC electron beam to establish a tight coincidence window for the signal. The detector, a large scintillation counter sensitive to very small energy depositions, provided much greater sensitivity than previous searches. Analysis of the data leads to the exclusion of a substantial portion of the charge-mass plane. In this report a preliminary mass-dependent upper limit is presented for the charge of milli-charged particles, ranging from $Q = 1.7 \times 10^{-5}$ at milli-charged particle mass 0.1 MeV/c^2 to $Q = 9.5 \times 10^{-4}$ at 100 MeV/c^2.

Presented at 23rd Annual SLAC Summer Institute on Particle Physics:
The Top Quark and the Electroweak Interaction (SSI 95),
7/10/1995-7/21/1995, Stanford, CA, USA

⋆ Work supported in part by the Department of Energy contract DE-AC03-76SF00515

1 Overview.

Particles with a charge $q \equiv Qe \leq 10^{-3}\, e$, with e the absolute value of the charge of an electron, are called milli-charged (mQ) particles. In the following sections, I will describe an experiment[1] that was performed at the Stanford Linear Accelerator Center during 1994 and 1995 with the objective of searching for such particles, and report preliminary results.

In section 2, I will briefly review what milli-charged particles are in more detail and why it makes sense to look for them. Some of the theoretical motivation[2,3] involves the concept of "shadow universes", but the main motivation for the experiment is the fact that milli-charged particles are not excluded experimentally in a large area of the mass vs. charge plane.[4,5,6,7]

Section 3 gives the presumed experimental signature for milli-charged particles, and explains why SLAC is an ideal location to search for them. A discussion of possible backgrounds follows, and the experimental setup is described in detail.

Section 4 describes the analysis, and in section 5 I present preliminary results.

2 What are milli-charged particles?

In general, milli-charged particles are particles with a charge $q \leq 10^{-3}\, e$. In the following, I will often use the abbreviation "mQ" to mean "milli-charged" or "milli-charged particle". The experiment I am about to describe in the following is, however, only sensitive to certain types of mQ particles.

For one thing, it is assumed that mQ's have only electro-magnetic and gravitational interactions, i.e. they are not subject to weak or strong interactions. This restriction is more or less a natural consequence in a model due to Holdom, which I will discuss later.

For another, our experiment was only sensitive to mQ masses $\lesssim 100\, m_e$. And further, in order to reach our detector, mQ particles have to be stable or at least long-lived.

2.1 Why look for them?

The primary reason to look for mQ particles is because they have so far not been ruled out by experiment.[4,5,6,7] They are also not forbidden by established physical principles. In fact, charge quantization is poorly understood and there is no a-priori reason to assume that all particles need to have a charge that is an integer multiple of $e/3$. The Standard Model can accommodate particles of arbitrary charge.

While it is true that most theories with super-symmetry require charge quantization at the fundamental level, there are mechanisms[3] by which mQ particles can be constructed (see the next subsection) without violating charge quantization.

Finally, if mQ particles exist, they might be a viable candidate for dark matter in the universe.

2.2 Shadow universes.

Holdom[3] has shown that mQ particles will arise naturally, and without violating charge quantization, in certain models involving what are called "shadow universes".

Imagine that there exist particles that to first order do not interact at all with the known matter in the universe, except gravitationally. Such particles might interact with each other in a similar way as the particles we all know. Such particles are generally known as "shadow particles", and the collection of them and their interactions makes up a "shadow universe". Supposing there is a shadow-U(1) gauge group for these particles, it follows there is such a thing as a shadow photon (sometimes called a paraphoton).

Of course, it would be impossible to detect these particles if there were no interactions between regular particles and shadow particles at all. One way of introducing higher-order interactions is through postulating the existence of particles which carry both regular charge and shadow charge. If these dual-charge particles were light, then shadow matter would interact easily with regular matter, so in the model they are heavy, with masses near the unification scale. Then one can have diagrams as in figure 1: a regular electron and positron annihilate into a regular photon, which turns into a loop of these dual-charge particles, which then turns into a shadow photon, which produces a pair of shadow particles. Of

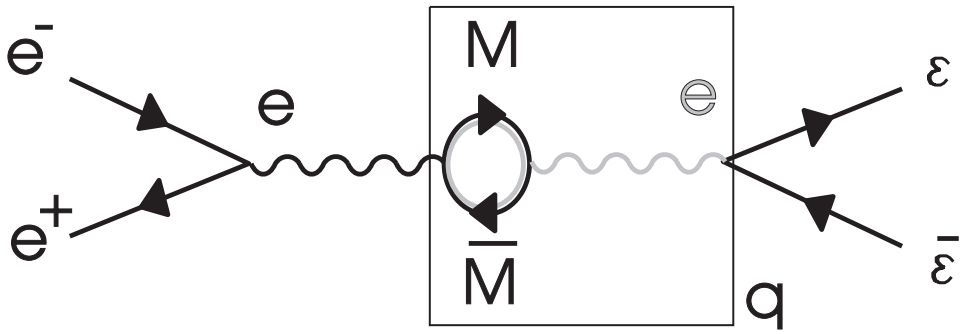

Figure 1. A photon mixing with a shadow-photon according to Holdom's mechanism.

course, if the mass of the intermediary is very large, the process would be very unlikely to occur.

The interesting thing about Holdom's model is that if there exist two types of such dual-charge particles, then there will be an interference between the two possible diagrams, and it turns out that the amplitude for the process involves the ratio of the two masses, and with suitably chosen values, the process would be more likely to occur.

One can treat the diagram of figure 1 in a simple manner. It so happens that in calculations, the regular photon coupled to the loop of intermediaries turning into a shadow photon coupled to the shadow particle pair, acts like a regular photon coupling to the shadow-particle pair at reduced strength. In other words, the part of the diagram in figure 1 enclosed by the box can be replaced by a reduced coupling strength for that vertex, $q \equiv Qe$, with $Q \lesssim 10^{-3}$.

The basic production mechanism for milli-charged particles is then of the Bethe-Heitler type as shown in figure 2. Note the absence of the usual other diagram—it is of higher order in Q and therefore unimportant. Similarly, the detection mechanism (shown schematically in figure 3) is the excitation of an atom or molecule by the energy deposited by a milli-charged particle, and the subsequent deexcitation in the form of detectable photons. The amplitudes for both production and detection therefore go as Qe, and therefore the total cross section for production and detection combined goes as Q^4.

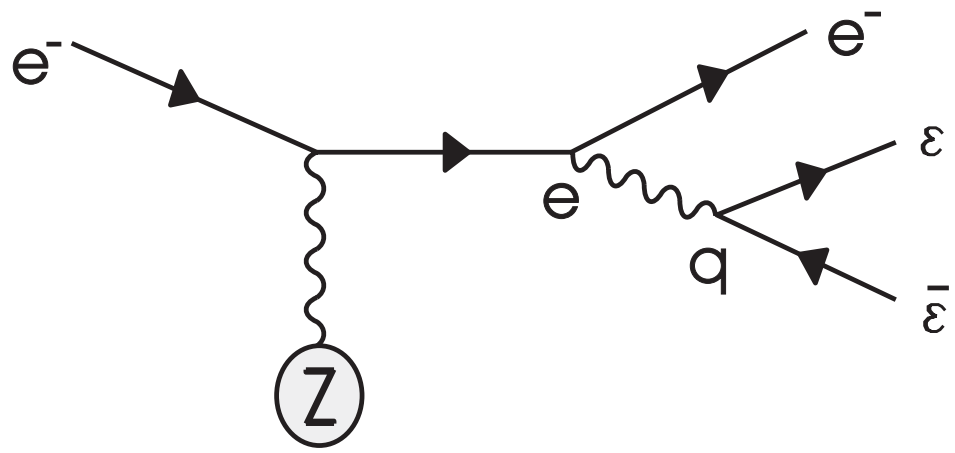

Figure 2. Leading diagram for mQ production.

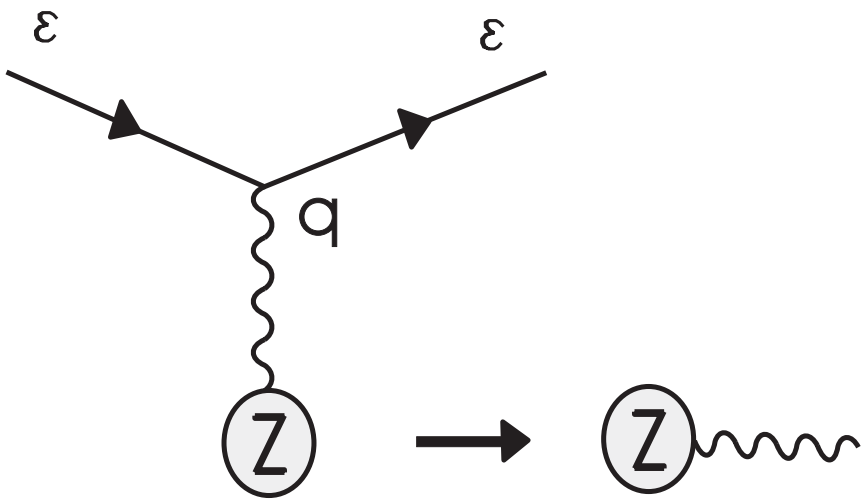

Figure 3. Schematic representation of mQ detection.

2.3 Unexplored regions.

Figure 4 shows a graph of charge vs. mass and shaded regions of charge-mass combinations that have been excluded so far by other experiments.[4,5,6,7] Shown are regions excluded due to the most precise measurement of the Lamb Shift, and three regions excluded because of particle physics experiments: Mel Schwartz's SLAC Beam Dump experiment, the Fermilab E613 experiment, and the ASP Free quark search. The reinterpretation of the available data for the purpose of the

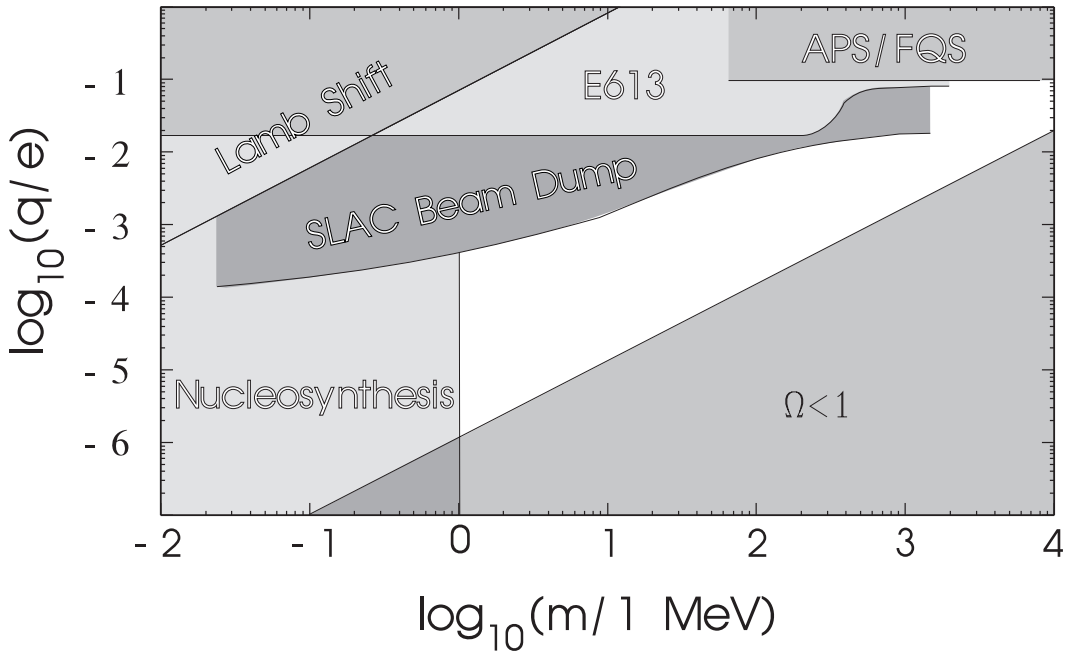

Figure 4. Currently excluded regions in the charge vs. mass plane.

graph was performed by S. Davidson et al.

Also shown are two regions excluded based on cosmological grounds. Masses below 1 MeV are excluded because of the effect the existence of mQ particles would have on nucleo-synthesis: if mQ particles had a very small mass, they would have caused the universe to have cooled more rapidly, and nuclei would have started forming earlier, giving fewer free neutrons the chance to decay, which in turn would give rise to a higher He abundance than is currently observed.

The large triangular region at small charge and large mass was calculated with the assumption that the universe is not over-closed, i.e. $\Omega \leq 1$.

Neither of the cosmological bounds is especially firm.

Clearly, there exists a large region between charges of 10^{-3} and 10^{-6} and masses between 1 and 1000 MeV, where mQ particles have not been excluded.

3 The experiment.

The experiment reported[1] here ran in 1994 and 1995 at the Stanford Linear Accelerator Center. Essentially, the experiment can be categorized as a beam dump experiment, with the SLAC positron production target serving as a beam dump. The experiment was "parasitic" in the sense that it did not require dedicated beam time. Rather, whenever positrons were produced in the course of normal SLC operations, the experiment took data.

3.1 Signature.

In such a beam dump experiment, where high-energy (29.5 GeV) electrons strike a target and produce light particles through a Bethe-Heitler-like mechanism, the particles will emerge near 0° with respect to the electron beam direction.

If the particles produced have milli-charge, they are expected to produce very little excitation and ionization in a detector. In a scintillator, they will produce only a single photon, leading to a single photo-electron detected in the photo-multiplier.

For the same reason, mQ particles will travel through a large amount of material without losing much energy.

3.2 Why SLAC?

SLAC is ideal for a mQ particle search for several reasons. For one thing, beam-time is essentially free because of the near-continuous use of the positron production target. For another, the pulsed nature of the SLC operation causes mQ particles to arrive at the detector at very precisely determined times. And finally, since the SLC pulse is so short, the time window within which mQ particles arrive at the detector is very small.

Overall this leads to a very good signal-to-noise ratio. In addition, it is easy to estimate the background, simply by measuring it slightly before and slightly after the expected arrival time.

3.3 The experimental setup.

The experiment consisted of a main scintillation detector 107 meters downstream of the positron production target, situated in a cylindrical 12-foot-diameter 22-foot-deep pit which was excavated from the surrounding sandstone. In addition, a set of five scintillation panels, arranged in a cross, was located 85 meters downstream of the positron production target, lowered to beam level in 1-foot-diameter holes drilled for the purpose.

A top view of the arrangement is depicted in figure 5. Shown are the accelerator itself, the positron extraction line, the positron production target, and the mQ experimental area. In the insert, the experimental area is shown in more detail: there are 7 1-foot-diameter holes arranged in a line perpendicular to the beam line. These are called E1 through E7. Of importance to the experiment are only E1, E2 and E3. E1 is located on the beam line. Also in-line with the beam line are holes P1 through P6. The main detector was located in P6. The trailer housed most of the electronics, and the data-acquisition system.

Figure 6 shows a head-on view of the 5 smaller scintillation panels. This setup was close enough to the positron production target that the highest energy muons were just barely able to reach these counters. The arrival time t_0 of muons was measured at E1, and the muon direction with respect to the nominal beam direction was determined using all 5 counters. They also provided a cross check for the luminosity determination, and a measure of the alignment of the setup with the beam direction. Figure 7 shows a graph of muon flux versus deviation from the 0° beam line. For this particular measurement, the holes E4 and E5 were also used. The data points are fully consistent with a gaussian shape, completely due to multiple scattering of the muons, as expected from EGS calculations.

A side view of the experimental setup is shown in figure 8. The electron beam strikes the 6-radiation-length tungsten target, and the produced muons and mQ particles enter the sandstone after about 24 meters (80 feet). Muons will still reach the muon counters in the E-holes at 85 meters (280 feet, shown is only hole E1), and mQ particles are the only ones able to reach the main detector in hole P6 at 107 meters (350 feet).

The main detector is shown in figure 9. It consists of a set of four 8.25" x 8.25" x 54" blocks of plastic scintillator (Bicron 408), each with a shaped scintillator light guide glued to one end and equipped with an 8" hemispherical (Thorn-

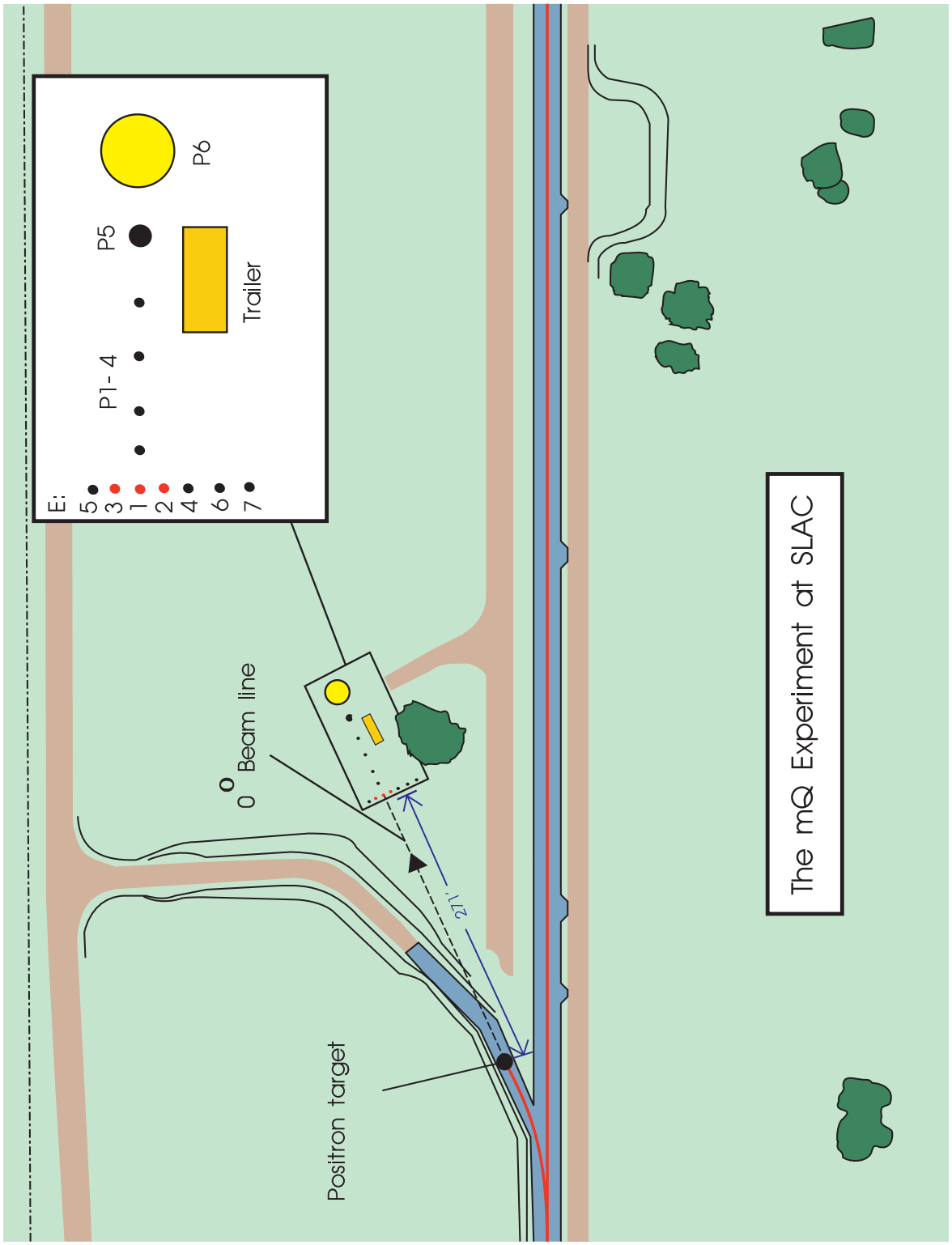

Figure 5. Top view of the mQ experimental setup.

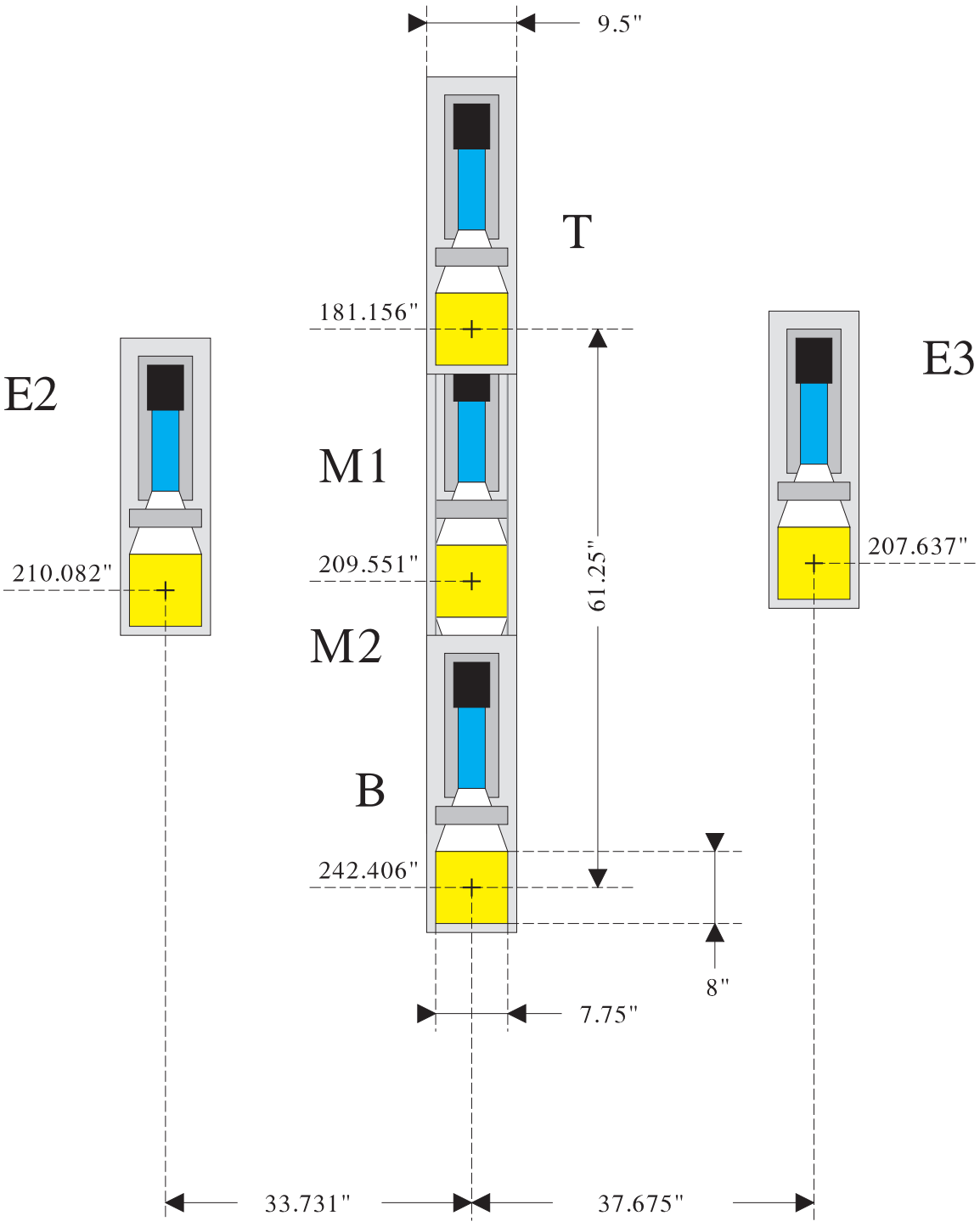

Figure 6. Head-on view of the 4 smaller scintillation panels used for muon detection.

EMI) photo-tube. Each block is wrapped in aluminum foil and plastic, and is surrounded by copper sheeting, serving as an isothermal surface during cooling.

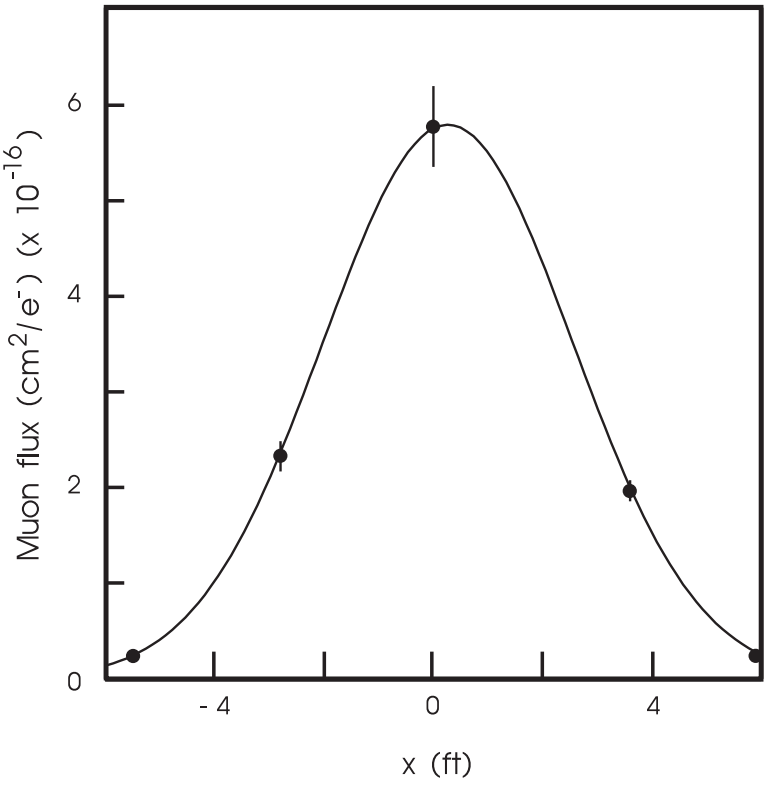

Figure 7. Number of muons as a function of lateral distance from the muon beam axis.

The four assemblies are contained in a Lucite box, which in turn is situated in a copper container which could be cooled to $-20°$ C. Surrounding the copper box were a 6" layer of thermal insulation and a 4" layer of lead shielding. Each counter was also equipped with an LED for calibration purposes. A pneumatic device allowed a radioactive source to be put inside the copper box by way of a tube, again for calibration purposes.

The signal from each of the four photo-tubes, which were run at relatively low voltage, was split into two signals, one of which was fed into a low-noise $\times 40$ amplifier. Both signals were connected to an ADC, with one ADC channel measuring the full spectrum of pulse-heights using the raw signal, while the other measured the low pulse-height spectrum from the amplifier in detail. The amplified signal was also fed into a discriminator and read out by a TDC, in order to measure the arrival time of the signal.

A schematic of the data acquisition is shown in figure 10. Analog signals from the experiment were digitized using CAMAC TDC's and ADC's. The CAMAC

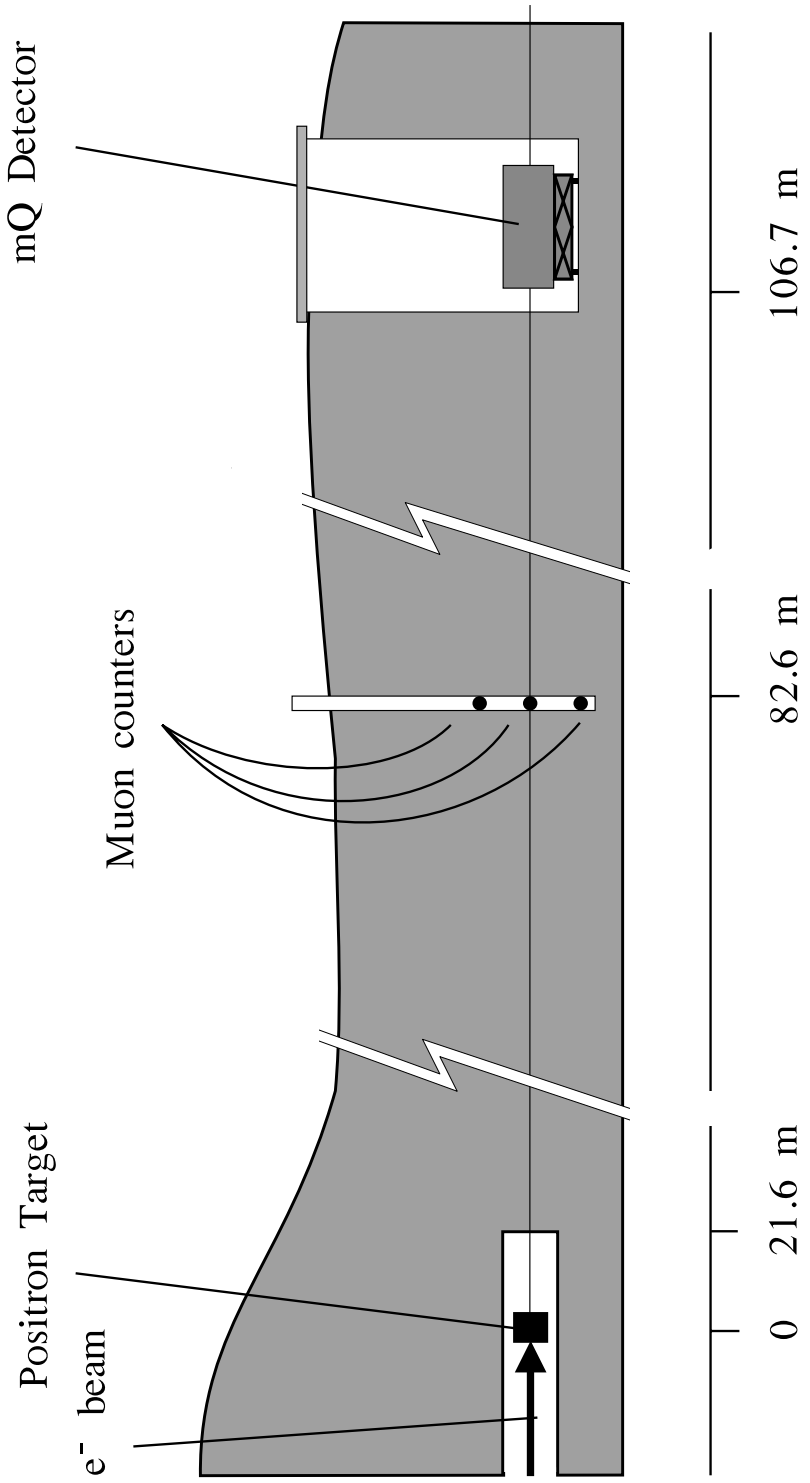

Figure 8. Side view of the mQ experimental setup.

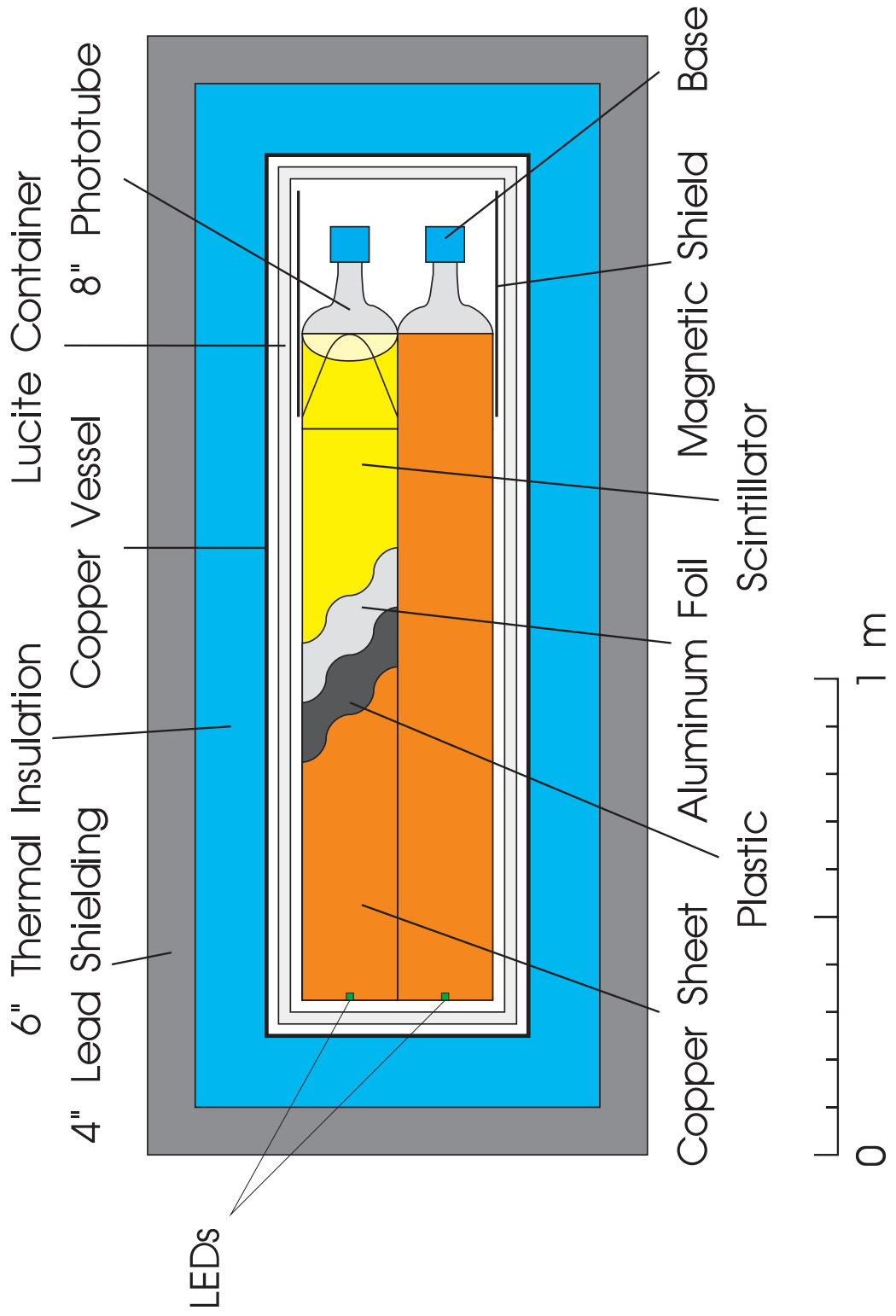

Figure 9. Schematic of the mQ main detector.

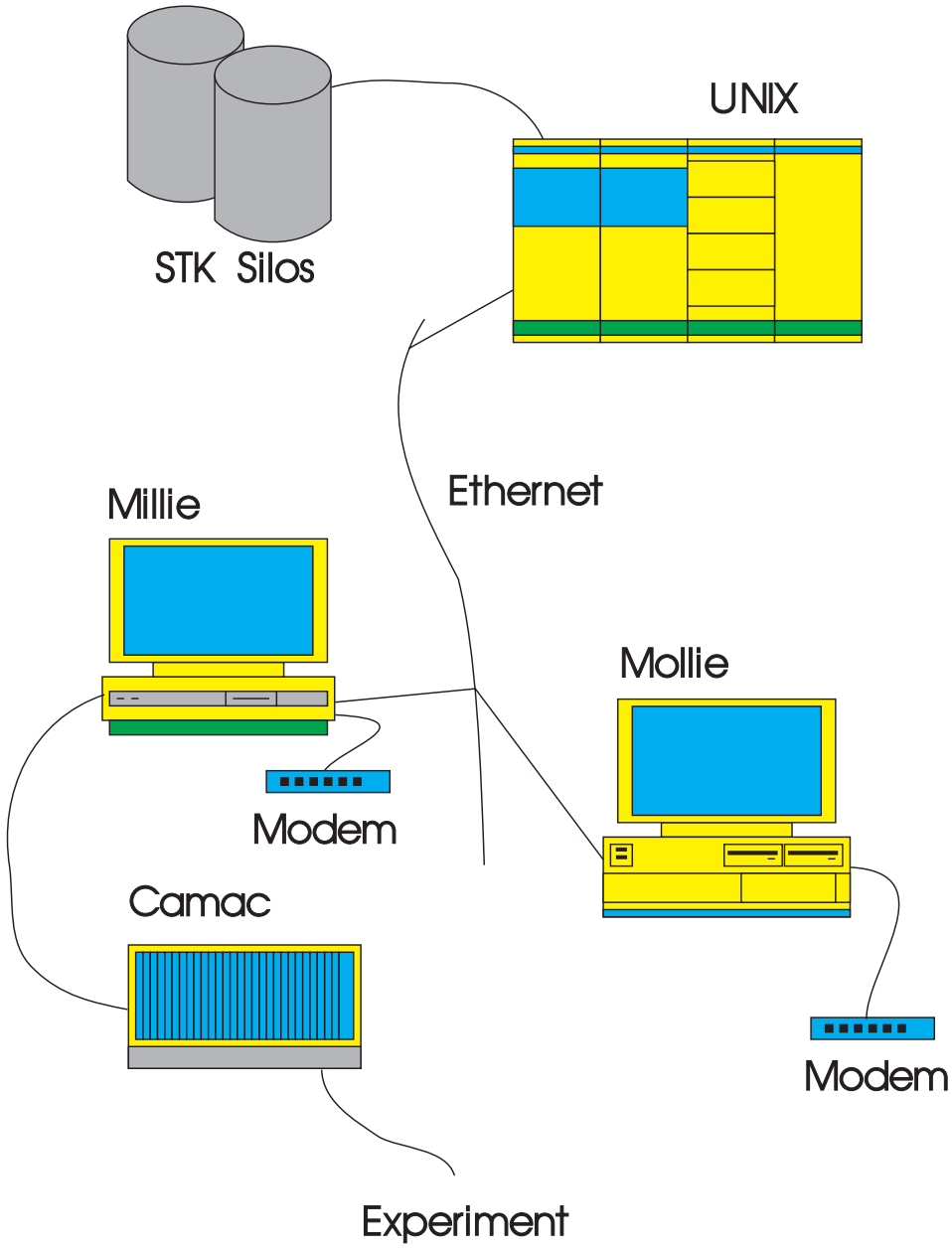

Figure 10. Representation of the mQ data acquisition system.

system was read out by an Amiga 3000T/040 personal computer (Millie), and the data were logged to a large hard disk. When the disk filled up, the data were offloaded through a fiber-optic Ethernet line to one of the SLAC central UNIX systems, and from there the data were written to tapes in the robotic tape silos.

The data-acquisition system continuously updated a large number of on-line

histograms, which were examined at the end of the run for any anomalies. Signals from the SLC control system were also read in through CAMAC, in order to measure certain machine parameters. In addition, certain records from the SLC controls database were transmitted from the main SLC computer to the data-acquisition computer, and merged into the data stream, allowing monitoring of the beam parameters during off-line analysis.

The data-acquisition computer was equipped with a modem, and would send messages to the pager of the person on shift if something went wrong. A second Amiga computer (Mollie) was also equipped with a modem and monitored the status of the main computer. If the main computer went off-line for any reason, the second computer would page the person on shift. It was therefore possible to run the experiment without anyone in attendance. Typical runs lasted about 24 hours.

3.4 Backgrounds.

The main background in the case of our large scintillator detector turned out to be to scintillator luminescence, the source of which has not been completely pinned down.[8] The current hypothesis is that events that produce a lot of light in the scintillator (mostly cosmic rays) cause the scintillator to emit photons for a long time afterwards. This is a much larger source of noise than the thermionic noise from the tube itself, which were selected for their low noise characteristics to begin with. Another problem due to the large amount of light from cosmic rays is tube afterpulsing. Cooling the entire counter to about 5° C reduces scintillator luminescence somewhat. A hardware veto was installed to reduce noise from afterpulsing by almost a factor 10, at the cost of introducing a tolerable ($\approx 30\%$) deadtime.

Cosmic rays themselves are not a source of background, because of the small coincidence window with the beam arrival time, and the fact that the pulse height recorded from any cosmic rays is so much larger than the single photo-electron scale expected for milli-charged particles.

Natural radioactivity from the surrounding sandstone is a source of background, but with 4 inches of lead shielding and the copper box surrounding the detector, this background is small in general, and negligible in the SPE region (the typical signals from natural radioactivity are much larger).

Other potential backgrounds, such as neutrons, coming straight from the target or scattered from the atmosphere ("skyshine"), neutrinos, and gammas from muon radiation, have been calculated and/or measured to be negligible.

One important feature of the experiment is that the background can be measured accurately: data obtained out-of-time with the beam arrival time is a good measure for the background, and as a check the experiment was repeated with the detector taken out of the beam.

4 Data analysis.

4.1 Luminosity.

The experiment took data from August of 1994 to April of 1995, at an incident electron beam energy of 29.5 GeV. The number of electrons per beam pulse was of the order of 3.0×10^{10} under good beam conditions. In order to keep track of the integrated luminosity, the digitized current of a toroid in the electron beam line as well as the number of muons detected in muon counter M1 was recorded. The results presented here represent a (dead-time corrected) integrated luminosity corresponding to 1.03×10^{19} electrons on target.

4.2 Production and acceptance.

The number of mQ particles produced per electron on target was calculated using a Monte Carlo QED calculation written by M. Swartz. The calculation included the effects of electron showering in the 6-radiation-length tungsten target. A numerical integration was then performed in order to determine the fraction of mQ's within the detector acceptance. It was further assumed that for small enough Q, the results scale with Q^2.

4.3 Detection.

The number of photo-electrons produced was calibrated by comparing the pulse-height spectra recorded for Co, Cs and Am sources with EGS simulations. An additional calibration point comes from cosmic rays.

From the above, photo-ionization and δ-ray fractions were calculated that produce a single photon at $Q = 10^{-3}$. The results were then extrapolated to lower Q assuming a Q^2 dependence.

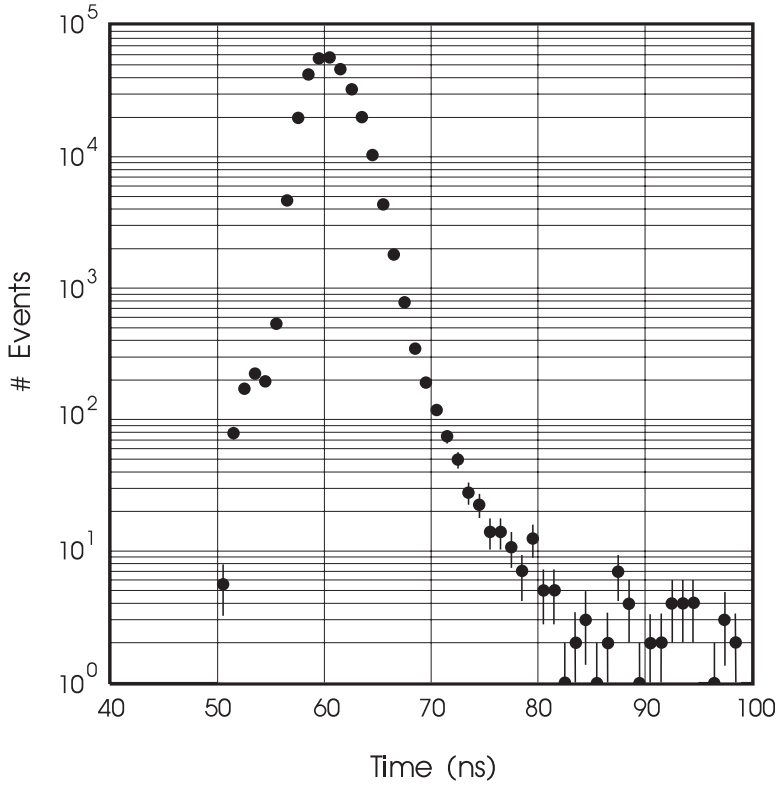

Figure 11. Typical time spectrum of muons arriving in M1.

4.4 Arrival time in the detector.

The arrival time t_0 of mQ's in the detector was arrived at in the following way. The arrival time of muons in muon counter M1 was 60 ns after the SLC reference signal used for this purpose. The time spectrum of muons arriving in M1 is shown in figure 11. The time of flight from M1 to the middle of the mQ detector is 90 ms at the speed of light.

A correction needs to be made to account for the differences in the lengths of the cables from M1 and the mQ detector to the trailer. These cable lengths were individually measured for M1 and each of the four mQ photo-tubes, and relative differences in the latter were taken into account. The overall correction is -33 ns.

An additional correction is needed to account for slewing: small signals arrive later than large signals. This effect was measured to be 16 ns. Figure 12 shows the setup used for the measurement: two small scintillators were used to make a cosmic ray trigger, and the light produced in one of the four main scintillators was measured by an 8" photo-tube. The measurement was done with the cosmic

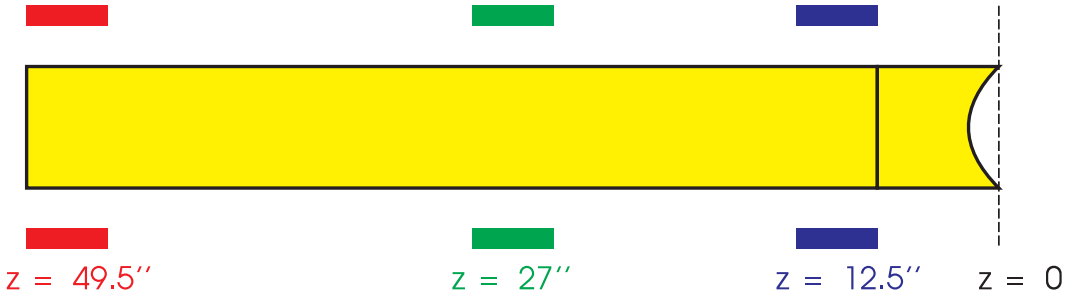

Figure 12. Setup for the small-signal timing measurement.

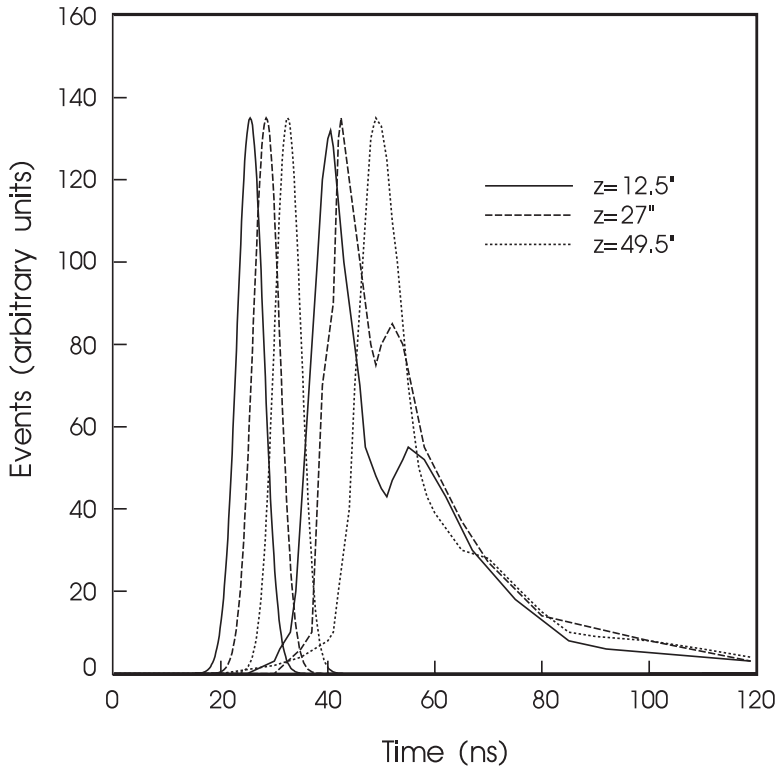

Figure 13. Differences in arrival time of small and large signals. The sharp early peaks are due to large signals (without filter), and the asymmetric broad peaks are due to single photons. The three different sets correspond to the three different measurement locations.

ray trigger in three different positions along the length of the detector. The set of measurements was repeated with an absorption filter in front of the 8" photo-tube, such that the light was attenuated to single-photo-electron level. The results are shown in figure 13. The sharp peaks at early times are due to the measurements

without filter, where the full cosmic-ray signal (tens of thousands of photons) arrived at the tube. The broad later distributions are due to the measurements with a filter.

Adding the various contributions (see figure 14), one arrives at $t_0 = 133$ ns.

4.5 Time window size.

The measurement of the time spectrum of single photons described above also shows that the resulting time spectrum is an asymmetric, broad distribution, which starts at about $t_0 - 7$ ns and ends at about $t_0 + 33$ ns. Of the SPE events, 85% fall within this range.

4.6 Spectra.

Figure 15 shows a density plot of pulse height as a function of the time, for the raw, unamplified pulse heights of one of the four counters. The cut-off at times above about 200 ns and pulse heights above channel 900 is due to the fact that large pulses that arrive late in the time window have part of their signal outside of the time window, resulting in a lower measured signal size. Aside from this effect, the spectrum looks the same for all times. A projection onto the pulse-height axis is shown in figure 16.

Figure 17 shows the density plot for the more interesting region of low pulse heights (measured using the $\times 40$ amplifier). The dark area between channel number 100 and 500 corresponds to the SPE peak. The darkness of each bin in figures 15 and 17 corresponds to the log of the number of counts in that bin. The horizontal dark band at the top of figure 17 is made up of overflows. The vertical dark band at about 20 ns corresponds to the ADC pedestal level. Aside from this, there is no significant time dependence. A projection of onto the pulse-height axis is shown in figure 18.

The time distribution of all events, summed over the four counters (after subtracting relative time offsets), is shown in figure 19. Note the offset vertical scale. A slight clustering of events near 150 ns is statistically insignificant. When a cut is made to allow only events with a pulse height between 2/3 and twice the nominal pedestal-subtracted SPE peak location (see figure 20), we arrive at the time spectrum shown in figure 21. Note again the offset vertical scale. The same clustering around 150 ns survives this cut, which keeps 72.5% of the SPE

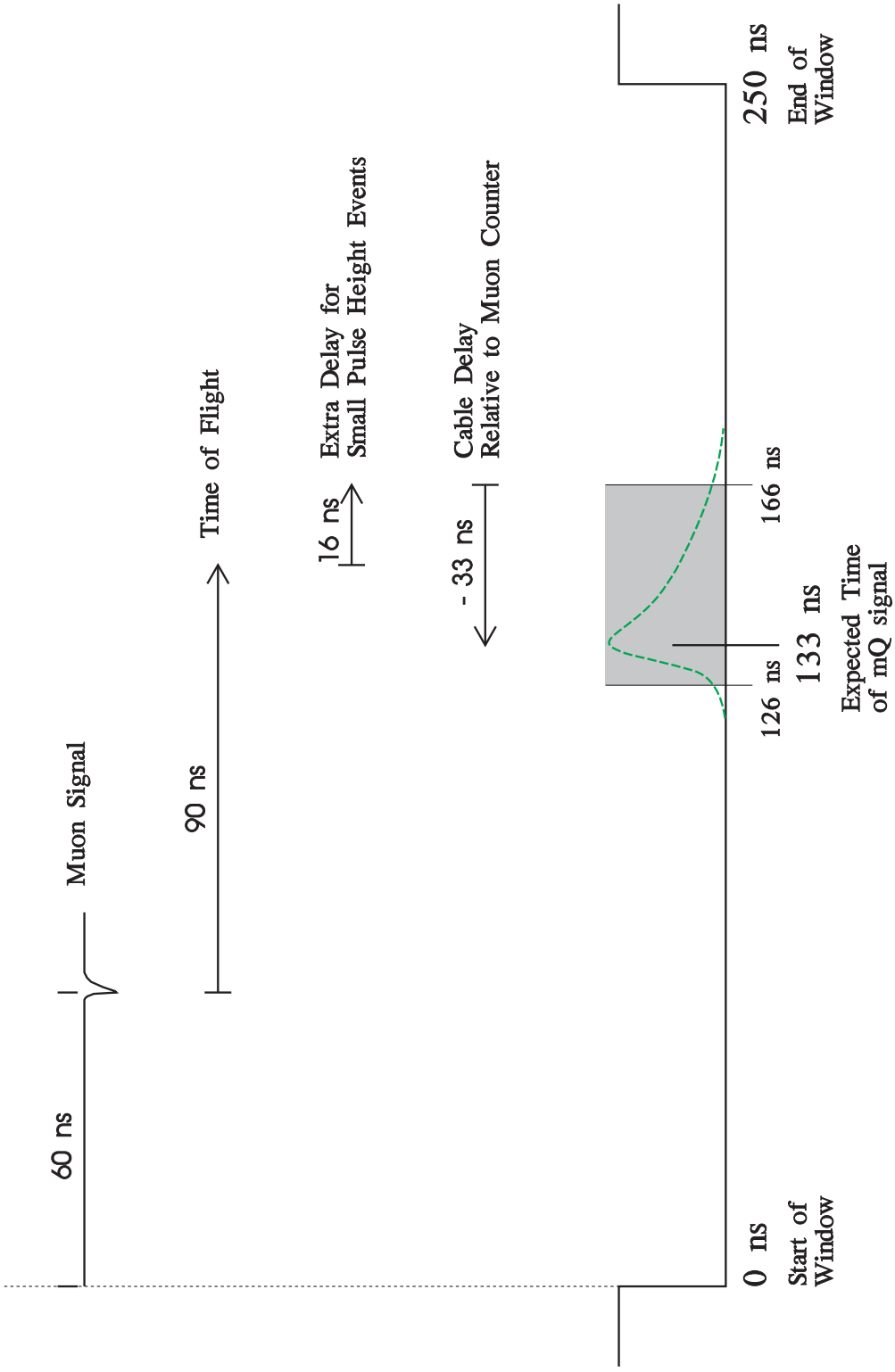

Figure 14. Diagram of the determination of the mQ arrival time.

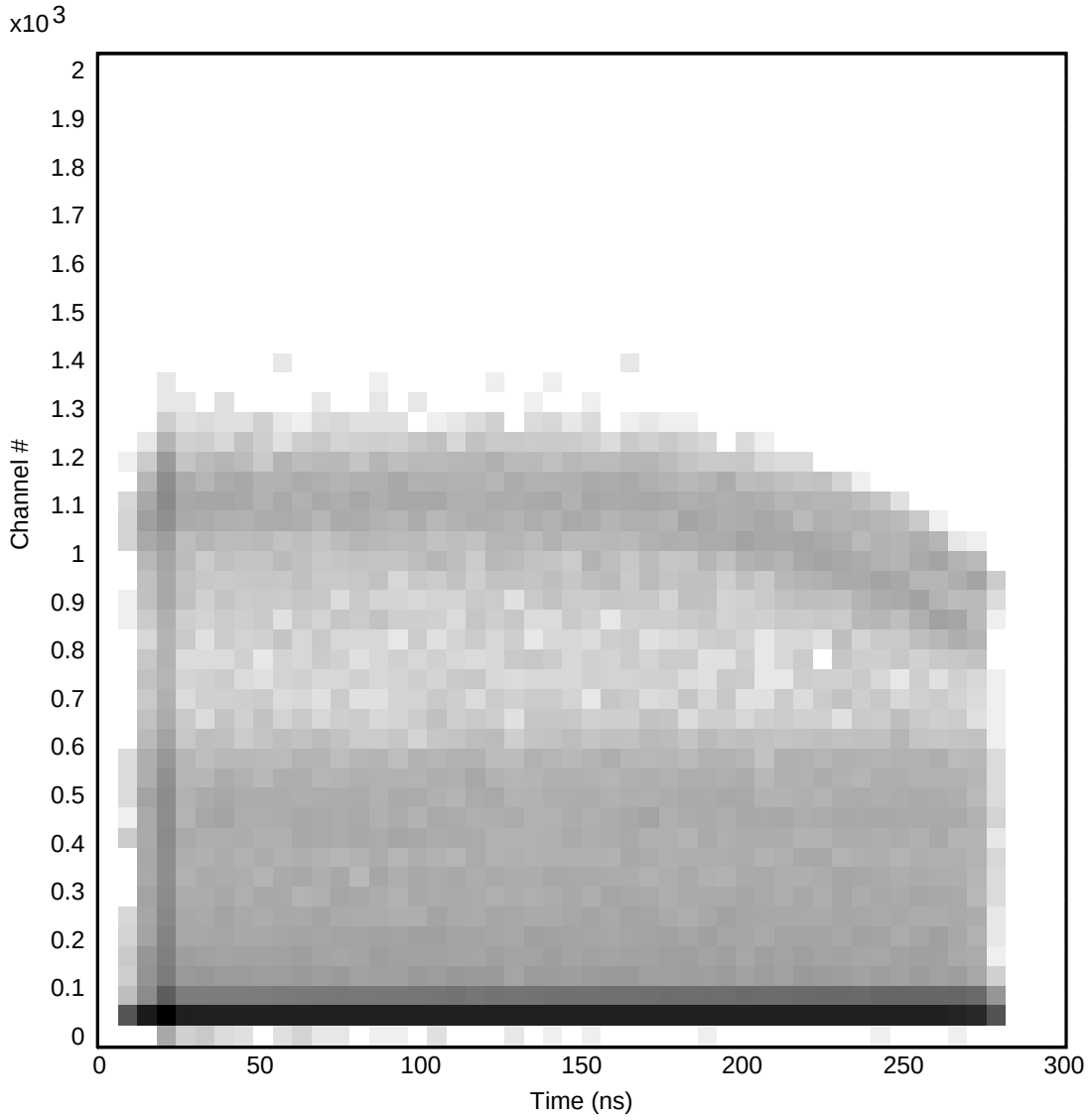

Figure 15. Density plot of the raw (unamplified) pulse height vs. time for one of the four counters.

events, but it is again not statistically significant. The overall upward slope of the spectrum is due to the asymmetric SPE cut: events with a pulse height below 2/3 SPE have a compensating downward-sloping time distribution. From other histograms, it is found that the spectrum of events that arrive early is shifted by a few channels toward lower pulse height compared to events arriving late. One likely explanation for this effect is that the signals are capacitively coupled to the readout electronics, and have an overshoot after the trailing edge of the signal.

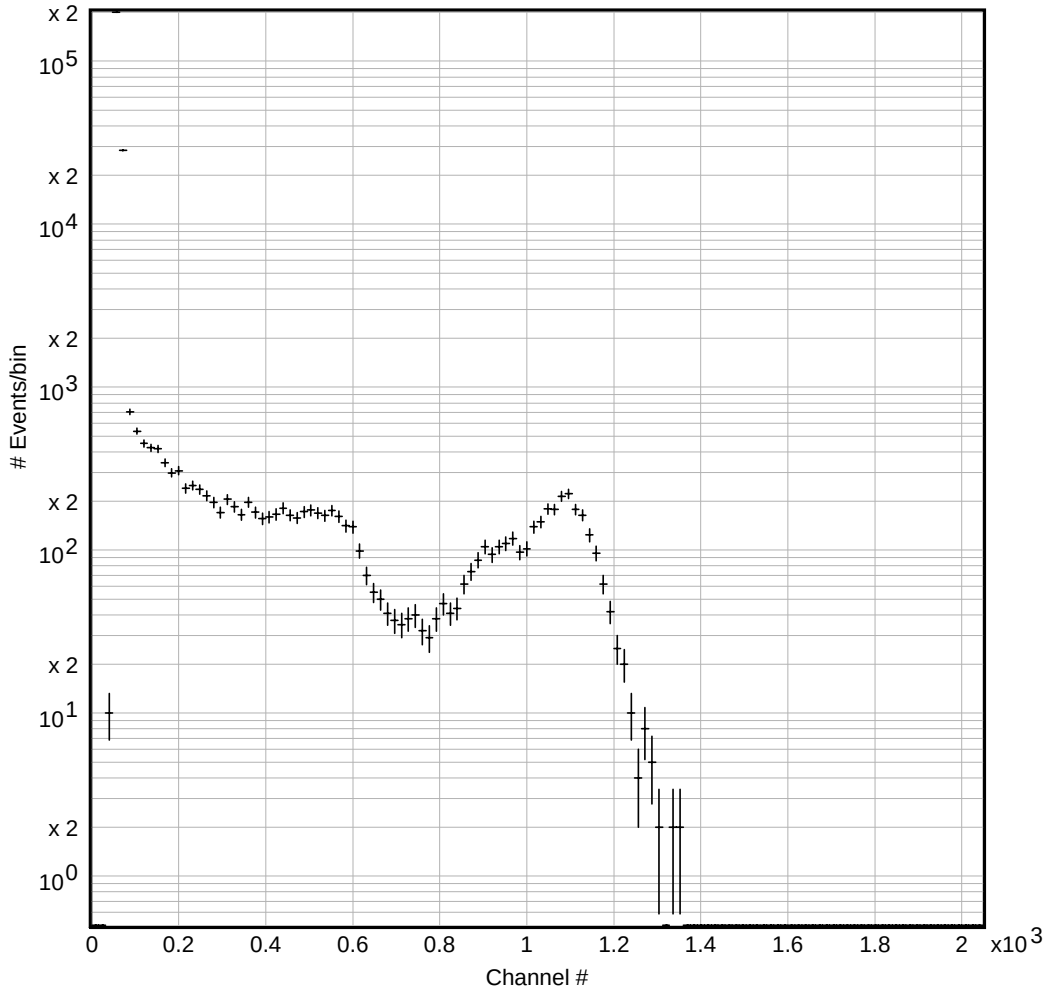

Figure 16. Number of events as a function of the raw (unamplified) pulse height of one of the four counters.

For early arrival times, more of the overshoot takes place within the time interval the ADC integrates over than for later arrival times. This effect is linear with time.

The vertical lines in figure 21 at 126 and 166 ns outline the calculated time window within which mQ events would appear. A fit was made to the data outside this region, in order to estimate the background inside the signal region. A straight line was found to be a good fit ($\chi^2 = 1.02$ per degree of freedom). There is no statistically significant excess above background in the signal region: the excess is less than one sigma above background in the 40 ns bin.

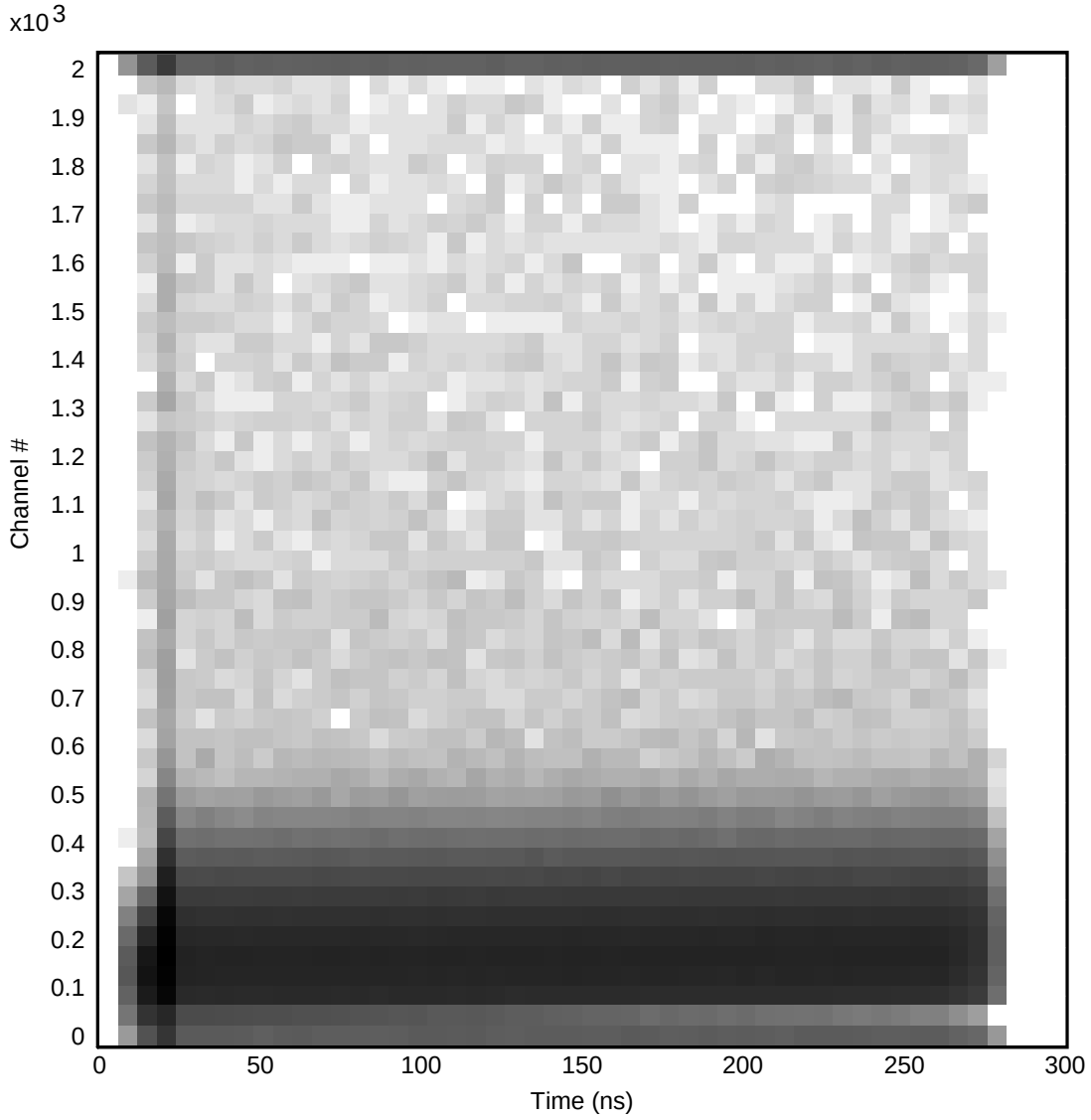

Figure 17. Density plot of pulse height vs. time, measured with the $\times 40$ amplifier, for one of the four counters.

4.7 Checks.

Various checks were made to insure the significance of the experiment. The alignment of the detector with respect to the beam was checked repeatedly and in different ways. The detector was less than 2 cm off-center during most of the running period.

The LEDs mounted on the four scintillators of the detector were pulsed at

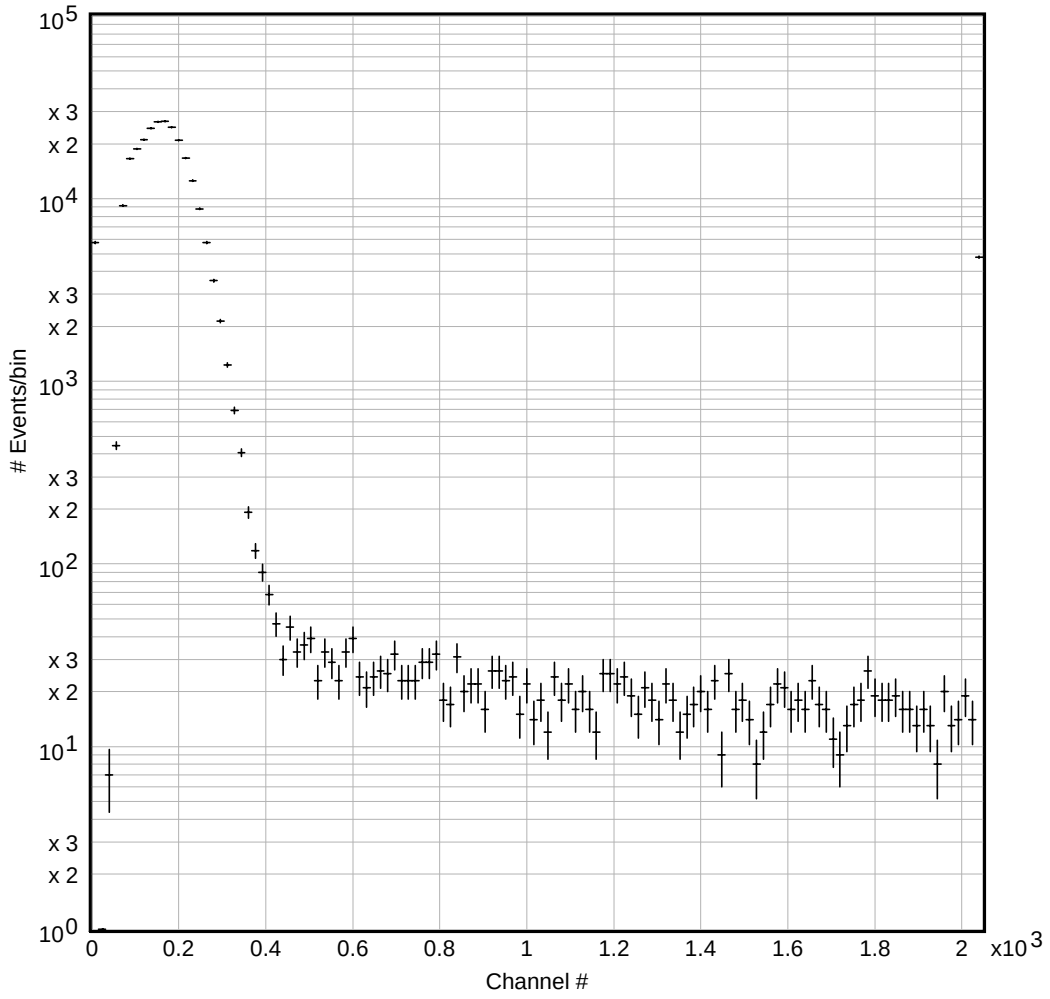

Figure 18. Number of events as a function of pulse height, measured with the $\times 40$ amplifier, for one of the four counters.

regular intervals, and the resulting events were recorded. These measurements proved that the counter was alive, that the time measurements were stable and that the timing resolution remained good, during the runs included in this analysis.

Measurements of the average Americium source pulse height from "source" runs, and the average position of the SPE peaks demonstrate that that the counters were sensitive and stable during this time.

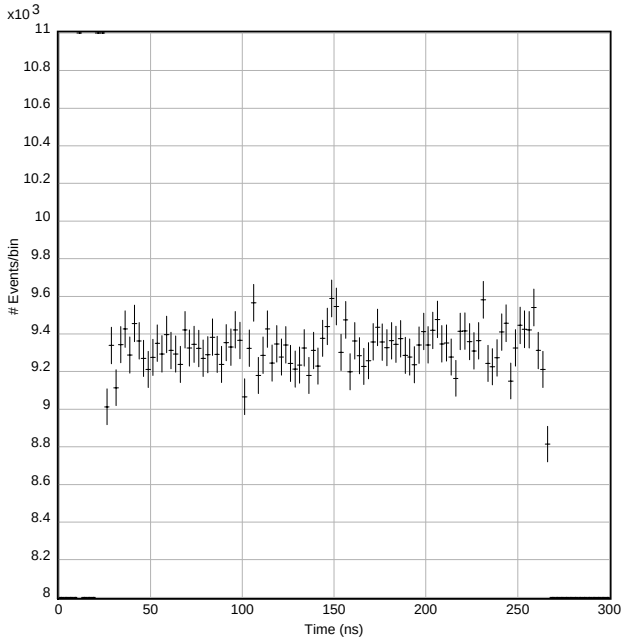

Figure 19. Time distribution for events of all pulse heights.

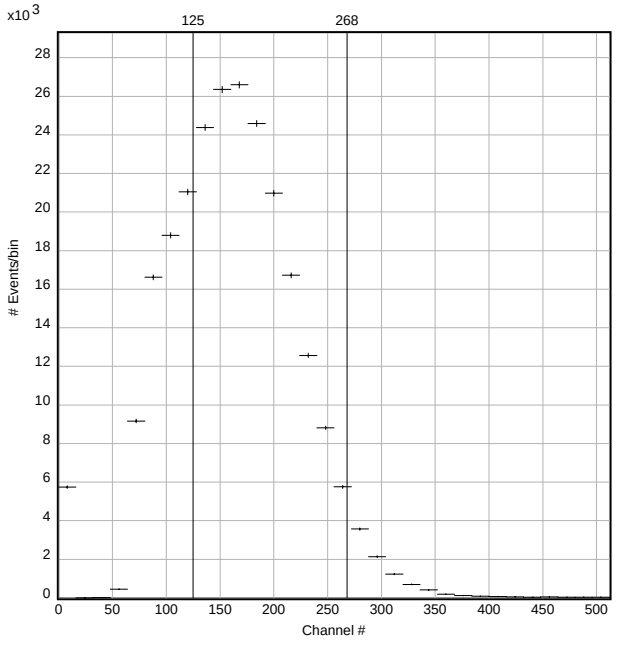

Figure 20. Single photo-electron peak. The vertical lines indicate the cuts on pulse height that were made in the analysis.

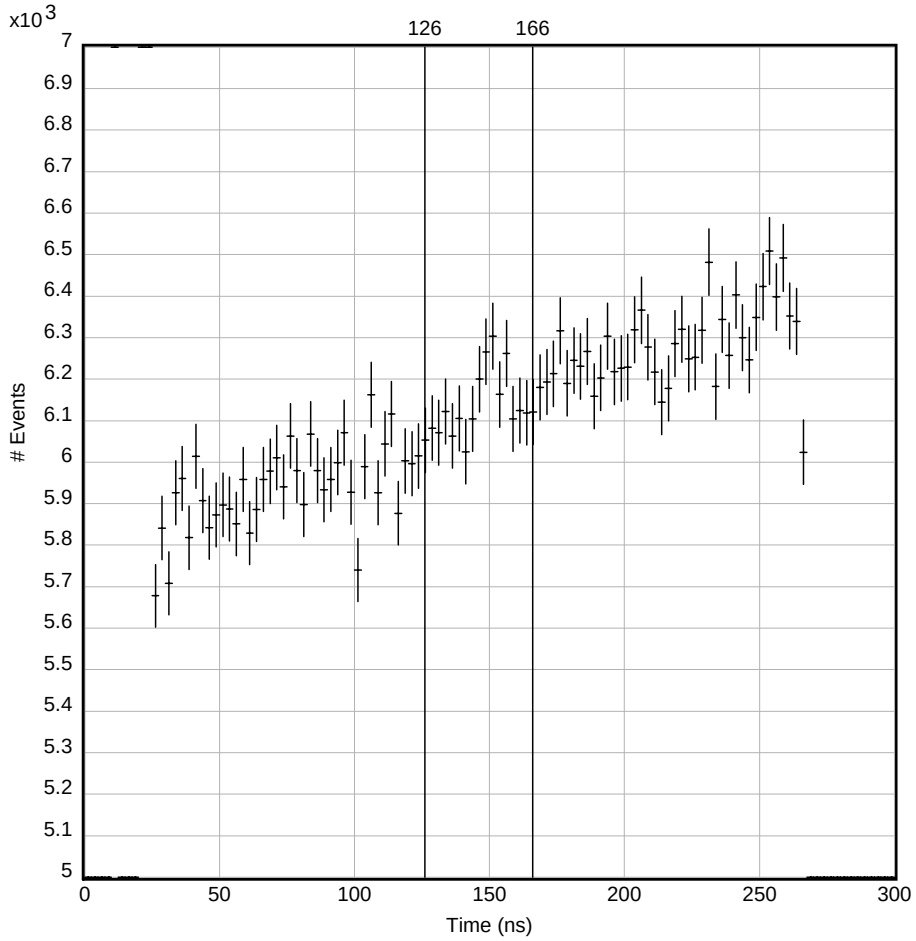

Figure 21. Time distribution for events for events in the SPE region.

4.8 Efficiencies.

As mentioned before, the SPE cut had an estimated efficiency of 72.5%. The limitation of the time window to a 40 ns interval around t_0 had an estimated efficiency of 85%.

4.9 Systematic errors.

In order to arrive at conservative estimates for upper limits, the following systematic errors were taken into account.

— The estimated systematic error in the current calculations of the production of mQ particles is a very conservative 50%.

— The estimated systematic error in the measurement of the luminosity is 10%.

— The estimated systematic error due to alignment uncertainties is 10%.
— The estimated systematic error due to uncertainties in the calculation of energy deposition is 10%.
— The estimated systematic error due to the calculated light yield is 20%.
— The estimated systematic error in the efficiency is 10%.

When added in quadrature, these contributions amount to an overall estimated systematic error of 57%. This number is of course dominated by the error in the calculations for mQ production. In the upper limit results that follow, the "worst case" production rate was assumed.

5 Preliminary results and conclusions.

The upper limit for the charge of mQ particles allowed by our measurements was now determined, for four different mQ masses, as follows.

First, the estimated background was subtracted from the data, to obtain the signal. All events in the signal region were summed, and the error σ in the signal was calculated. If the total signal (after background subtraction) was less than 0, the signal was taken to be 0 events. To this signal, 1.65 times σ was added in order to arrive at a 95% confidence-level upper limit.

This procedure was repeated for various different values of t_0, in order to check what would happen if for some reason our measurement of t_0 were incorrect, or if mQ particles did not arrive at the expected time. As an example, the 95% CL upper limit for Q is plotted vs. t_0 in figure 22 for a mQ mass of 1 MeV/c^2. As expected, there is a small peak near 150 ns, but the upper limit there is not significantly different from the upper limit calculated at the nominal value of $t_0 = 133$ ns, indicated by the vertical line in the figure.

The results of the experiment are summarized in figure 23. It shows the already-excluded regions mentioned before, and in addition the newly excluded region determined by this experiment. Specifically, the results for four different mQ mass values are:

m_{mQ} (MeV)	Q (95% CL)
0.1	$< 1.7 \times 10^{-5}$
1	$< 3.5 \times 10^{-5}$
10	$< 1.2 \times 10^{-4}$
100	$< 9.5 \times 10^{-4}$

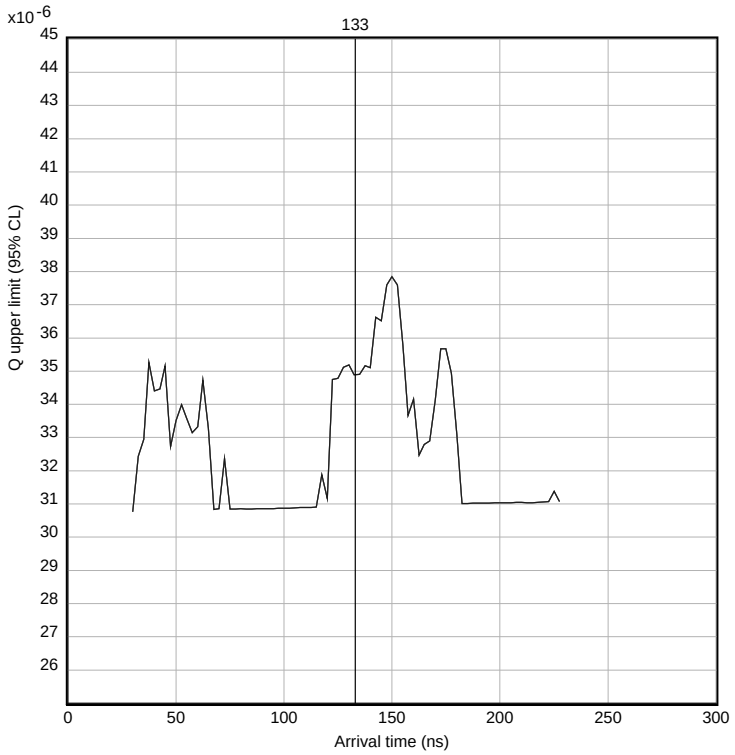

Figure 22. Upper limit on mQ charge for mQ mass 1 MeV, as a function of assumed arrival time.

Our detector is in principle sensitive to mQ masses above 100 MeV, but reliable limits have not yet been determined. We have also not yet computed an upper bound for the excluded region—our detector is not sensitive to large Q^2 ($Q \lesssim 0.2$), low-mass mQ's, because such particles would range out in the sandstone in front of the detector.

In conclusion, we have established preliminary upper limits for the fractional charge Q of mQ particles as a function of their mass. A significant fraction of the hitherto allowed region in the Q vs. mass plane was excluded.

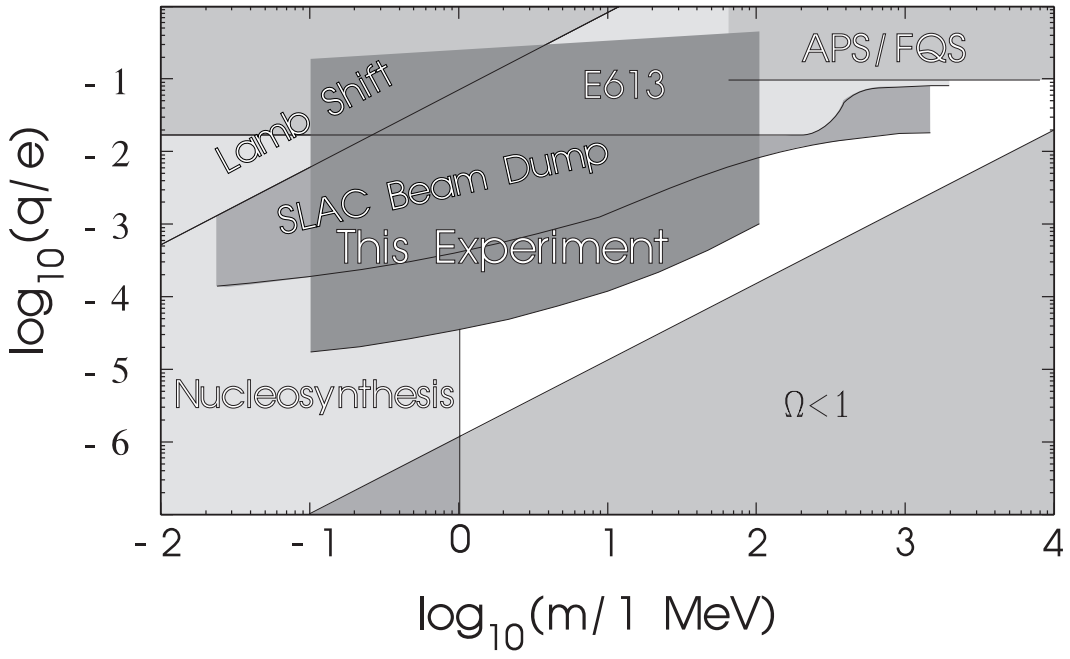

Figure 23. Preliminary results of this experiment. Shown is the newly excluded area, compared to the previously excluded regions.

References

[1] The members of the Milli-charged Particle Search Experiment at SLAC are: R. Baggs, J. Ballam, S. Ecklund, C. Fertig, J. Jaros, K. Kase, A. Kulikov, W. Langeveld, B. Leonard, T. Marvin, T. Nakashima, W.R. Nelson, A. Odian, M. Pertsova, A. Prinz, G. Putallaz, and A. Weinstein.

[2] A. Yu. Ignatiev, V.A. Kuzmin, and M.E. Shaposnikov, Phys. Lett. **84B**, 315 (1979).

[3] R. Holdom, Phys. Lett. **166B**, 196 (1986).

[4] M.I. Dobroliubov and A. Yu. Ignatiev, Phys. Rev. Lett. **65**, 679 (1990).

[5] S. Davidson, B. Campbell, and D. Bailey, Phys. Rev. **D43**, 2314 (1991).

[6] R.N. Mohapatra and S. Nussinov, Int. J. of Mod. Phys. **A7**, 3817 (1992).

[7] S. Davidson and M. Peskin, Phys. Rev. **D49**, 2114 (1994).

[8] Thomas P. Marvin, SLAC-PUB-95-7042 (1995).